ACSNANO

www.acsnano.org

ARTICLE

Real-Time Optical Measurements of Nanoparticle-Induced Melting and Resolidification Dynamics

Suhun Jo, William L. Schaich, and Bogdan Dragnea*

Cite This: *ACS Nano* 2023, 17, 505−514

Read Online

ACCESS | Metrics & More | Article Recommendations | Supporting Information

ABSTRACT: **The photothermally induced nanoscale dynamics of rapid melting and resolidification of a thin layer of molecular material surrounding a nanoparticle is examined in real time by an all-optical approach. The method employs pulsed periodic modulation of the medium's dielectric constant through absorption of a low-duty-cycle laser pulse train by a single nanoparticle that acts as a localized heating source. Interpretation of experimental data, including inference of a phase change and of the liquid/solid interface dynamics, is obtained by comparing experimental data with results from coupled optical−thermal numerical simulations. The combined experimental/computational workflow presented in this proof-of-principle study will enable future explorations of material parameters at nanoscale, which are often different from their bulk values and in many cases difficult to infer from macroscopic measurements.**

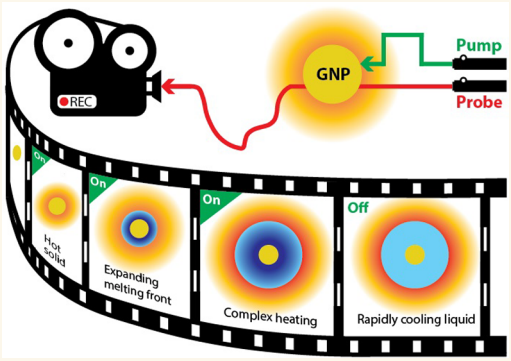

KEYWORDS: *photothermal microscopy, nanoscale melting, thermoplasmonics, heat transport, nanoheater*

INTRODUCTION

At nanoscale, the dominance of interfacial effects makes the thermodynamics of phase change processes, such as melting or crystallization, to be strikingly different from those of bulk matter.[1,2] Kinetic departures from bulk characteristics can translate into significant impact at macroscale. For instance, a gold nanoparticle (NP) solution can efficiently produce steam without boiling water when irradiated by light at resonant wavelengths.[3] Antifreeze proteins enable the survival of various organisms at subfreezing temperatures by leveraging interfacial control of freezing kinetics.[4] Finally, because of the interfacial energy dependence on local curvature, a life-sustaining, liquid water can be found at temperatures well-below freezing, under confinement in the pores of minerals and Arctic permafrost soils.[5]

The fundamental knowledge concerning such scale-dependent thermodynamic behavior has soared recently, powered by advances in theory and computation and structural analysis.[6,7] However, fully understanding phase transformations at nanoscale requires pathway analysis and considerations of transport processes (heat flow, viscosity, impurity flow) and thus time-course approaches capable of capturing dynamics with high spatial resolution. The advent of *in situ* electron microscopy (EM) has partially fulfilled this need for heavy-atom materials;[8,9] however, for light-atom molecular materials, real-time *in situ* EM is challenged by low contrast.

Because light-absorbing NPs can thermally initiate local physical or chemical transformations of the medium in which they are embedded and because thermal evolution can be very rapid in their vicinity,[10] they represent a natural choice for probing far from equilibrium phase transformations at nanoscale. Moreover, NP-assisted phase changes carry broad technological potential and environmental relevance.[11] For instance, both natural and synthetic NPs are believed to hold (and likely will further assume) a role in atmospheric phenomena.[12] They can travel high and far in the atmosphere and bias its feedbacks by catalyzing chemical reactions, triggering precipitation, and modifying the albedo of snow and ice to which they stick.[13] With the increased consideration garnered by geoengineering proposals seeking to mitigate the effects of climate change on global ecosystems,[14,15] it is important for NP-assisted thermochemical phenomena to be understood at a fundamental level and become part of the predictive geophysical modeling across scales. The same goes

Received: September 15, 2022
Accepted: December 15, 2022
Published: December 22, 2022

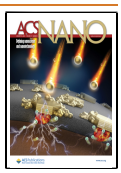

for NP-assisted phase changes employed in the development of high-performance thermal IR detectors,[16] of efficient therapeutic delivery and cancer treatment approaches,[17,18] of materials for smart, energy-saving building construction,[19] and of solar-powered water purification systems.[3]

Photothermal (PT) microscopy is a method uniquely adapted to the study of NP-assisted thermal phenomena.[20] In PT microscopy, a nanoparticle embedded in a transparent medium is irradiated by a time-modulated beam at a wavelength that is strongly absorbed by the NP but not the medium. Within microseconds, the heat resulting from optical absorption dissipates over a radius of the order of 100 nm into the medium. In the absence of a phase transformation, the density and the index of refraction of the medium change smoothly as a function of the temperature. Propagation of a probe beam passing through the heated zone over the duration of the transient thermal lens is influenced by it, with the result of a modulation in the detected power of the probe which is recorded and mapped as a function of spatial coordinates. Thus, in PT microscopy contrast is a function of the optical properties of the nanoparticle, as well as the thermo-optical properties of the material surrounding it. A particular implementation of PT imaging, photothermal heterodyne imaging (PHI) microscopy[21] has been widely employed due to its high spatial resolution[22,23] and sensitivity.[24−26] Most implementations employ a harmonically modulated heating beam and phase-sensitive detection (lock-in amplification). The sensitivity of the method comes from probing the thermo-optical response of the system in a narrow window around a single frequency, which is reasonable for a response that is known to be linear and nearly instantaneous with respect to the modulation kinetics.[27] However, when phase change phenomena are present, the transient scattering of the probe beam is not solely caused by smooth changes in the index of refraction due to temperature but also by the formation of sharp interfaces between phases of different density. The latter is expected to contribute significantly to the overall optothermal modulation of the probe-beam detected power. For instance, in water $dn/dT \approx 10^{-4}/°C$, while $\Delta n = n_{ice} - n_{water} = 10^{-1}$. In this case, if conventional single-frequency lock-in detection were employed, information contained in the harmonics of the signal would be lost. Thus, to study kinetics of transient phase change processes such as melting/refreezing in the vicinity of a NP, a methodology is required which (i) faithfully captures kinetics beyond steady-state regimes of thermal transport and phase changes and (ii) employs modeling feedback for data interpretation from thermo-optical numerical simulations that include a traveling solid/liquid front.

Previous studies of PT NP-assisted phase transitions dealt with microbubble formation in the liquid medium surrounding a light-absorbing NP.[28] The estimated size of the microbubbles was about 1 μm, and their lifetime was less than ~1 μs. This instance of rapid reversible microscopic phase change was later employed to increase the sensitivity of photoacoustic diagnosis and to aid in the therapeutic photothermolysis of tumor cells.[29] The change in the refractive index due to the phase transformation in this case being substantial, a less-sensitive broader bandwidth, lock-in free detection scheme can be employed for real-time observation. Hou et al. have shown that it is possible to follow in real time the formation and decay of nanobubbles of 100−200 nm estimated radius through an approach employing continuous heating of a single 80 nm NP in water, modulated at 10% duty cycle.[30] Expansion and contraction of the nanobubble occurred over tens of nanoseconds, a time scale that highlights the requirement for sharp temporal resolution. While nanobubbles have been already fairly intensely studied in relation with their potential for photothermal therapies,[31−36] no complete optothermal modeling has been put forward that could be directly compared against the observed optical transients. Nevertheless, such comparisons would be invaluable for the study of nanoscale thermokinetic parameters such as the Kapitza thermal boundary resistance, which was predicted to be a dominant factor at the onset of the new phase.[37]

Because of the large difference in the dielectric constant of the condensed phase and its vapor in the above studies, the question arises if differences between two condensed phases would be also detectable in real time. Parra-Vasquez et al. have taken advantage of the large index of refraction change occurring at a thermotropic liquid-crystalline phase transition to detect the PT induced phase change around 28 nm Au particles.[38] In a similar vein, an all-optical light modulator was introduced that uses a nanoparticle-assisted, photothermally induced phase transformation in a nematic liquid crystal film.[39] In a different approach, Zahedian et al. showed that the phase angle difference between the detected scattering and the heating modulation is a sensitive indicator of solid−solid phase transformations.[40] However, in these studies, kinetics of the phase change were obscured since detection was still via time-harmonic modulation and conventional lock-in detection. Therefore, until now it has remained unclear (i) whether the time evolution of a phase change from a solid to a finite-size liquid shell and back could be recorded using an optical approach similar to the one in ref 30 and (ii) if it would be possible to extract various parameters of the phase transformation (extent, nucleation, hysteresis, melting front velocity, etc.) from comparisons with simulations of the time-evolution of the optical signal. The work presented here seeks to begin answering these questions.

Using low-duty-cycle pulsed heating and a lock-in free optical detection scheme, we show that heat dissipation from Au NPs embedded in a stearic acid film induces the transient melting of a thin shell of the molecular material surrounding the particle. We follow the time evolution of the melting and refreezing process with better than 1 μs time resolution. To interpret the observed time evolution of the optical scattering signal, we employ coupled thermo-optical numerical simulations wherein the detected optical scattering power is calculated at each time step from the distribution of temperature and phase-dependent dielectric constant. The latter is obtained from numerical modeling of heat transport with phase change as a function of time.

RESULTS AND DISCUSSION

To ensure that we could produce enough heat to study phase transitions, we have used Au NPs 100 nm in diameter. In addition, at this size, NPs can be readily examined with wide-field epi- or dark-field microscopy prior to and after photothermal probing and addressed individually by the galvomirror steered heating and probe beams. See the Supporting Information Figure S1 for a schematic description of the setup.

For the embedding medium we chose stearic (octadecanoic) acid (SA), a saturated fatty acid frequently studied as a model organic soil pollutant in clays[41] and for thermal energy storage

https://doi.org/10.1021/acsnano.2c09212
ACS Nano 2023, 17, 505−514

Table 1. Thermal and Optical Properties of Stearic Acid ($C_{17}H_{35}COOH$)

physical state	density [kg/m^{-3}]	heat capacity [kJ/(kg·K)]	thermal conductivity [W/(m·K)]	optical refractive index	melting temperature [°C]	latent heat of fusion [kJ/mol]
solid	940.8[44]	1.9075[45]	0.41[46]	$1.534 - (2.397 \times 10^{-4} \times T\ [°C])$[47]	69.3[44]	61.208[45]
liquid	847.0[44]	2.26[48]	0.173[49]	$1.457 - (3.528 \times 10^{-4} \times T\ [°C])$[47]	69.3[44]	61.208[45]

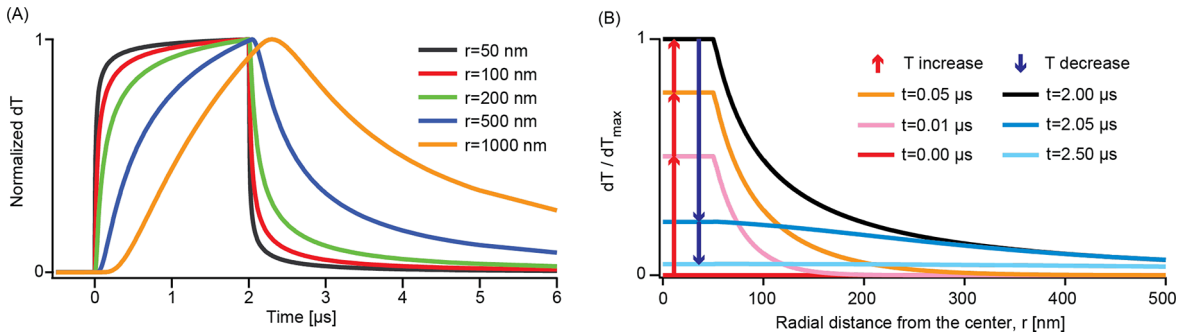

Figure 1. Calculations of the temperature evolution for SA in its homogeneous solid phase. (A) Time profile of the change of temperature, dT, at different radial distances, r. Each profile has been separately normalized so that its maximum is unity. (B) Spatial distribution of temperature changes during heating (red) and cooling (blue) at different times. The plateaus for $0 < r < 50$ nm are due to the nearly constant temperature through the NP. The dT values here are all scaled by the maximum temperature rise of the NP, dT_{max}.

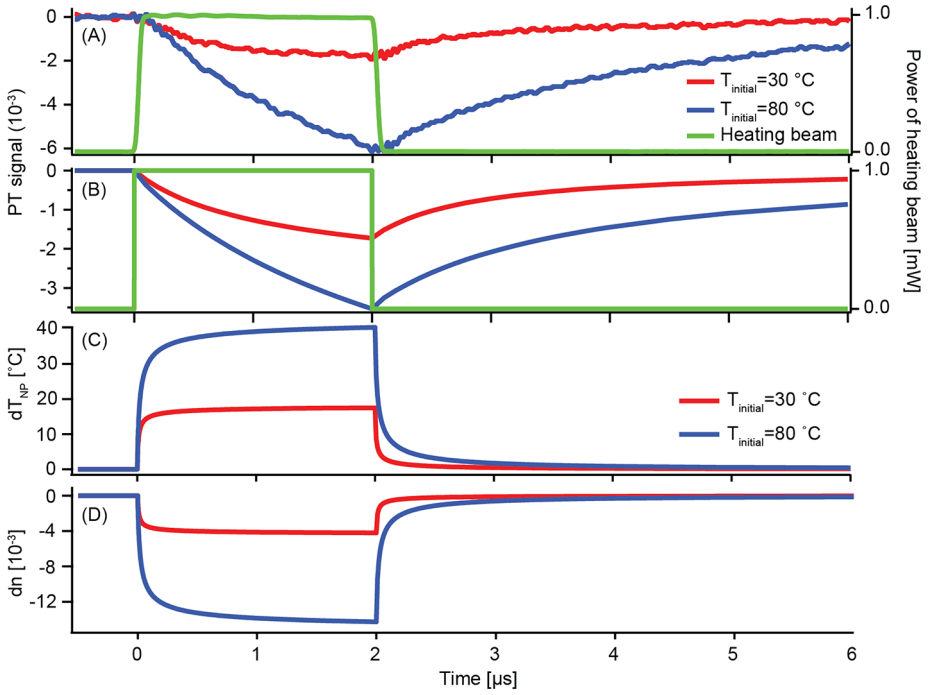

Figure 2. Comparison of transient thermal and optical responses in homogeneous SA (no phase change). (A) Experimental PT signal in solid (red) and liquid (blue). Heating time profile is in green. (B) Calculated PT signal for the same experimental conditions. (C) Time profile of the temperature change (dT_{NP}) in solid (red) and liquid (blue) at the NP/SA interface (r = 50 nm). (D) Change of optical refractive index at the same location.

materials applications.[42] Because of its technological relevance, its physical properties including optical and thermal transport are reasonably well-known.[43] Conveniently for our experiments, SA is transparent in the visible spectrum, and in crystal form it has a well-defined bulk melting temperature, Table 1. In calculations we have used T_{fusion} = 69.3 °C, which is the reported melting temperature for a crystalline solid, although depending on sample purity and crystallinity, a temperature range of 67−70 °C is to be expected.[43] With SA as a medium melting/refreezing experiments can be conveniently done in the vicinity of room temperature, whereas other temperature ranges and materials would require increasing the complexity of the setup to mitigate the effects of condensation and/or strong static temperature gradients. The equilibrium (initial) temperature was controlled in experiments through the use of a microscopy stage with double-sealed nitrogen-filled chamber walls.

Figure 1 provides an initial look at simulation results, showing the typical evolution of temperature-change profiles in a homogeneous phase (solid SA) subjected to a square heating pulse of 2 μs duration. For simplicity, a small heating effect of the probe beam has been ignored here. The variable dT is

https://doi.org/10.1021/acsnano.2c09212
ACS Nano 2023, 17, 505−514

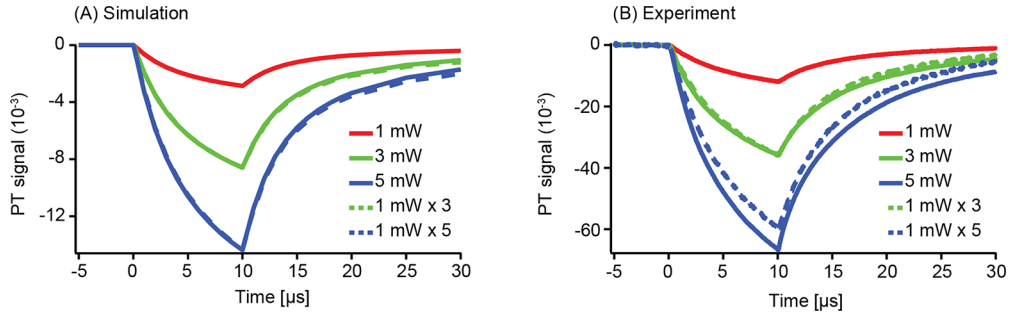

Figure 3. Comparison between the time-resolved PT signals measured at 1, 3, 5 mW (solid lines) and amplified signals by multiplying the signal at 1 mW by 3 and 5 (dashed lines), in homogeneous liquid state SA, (A) from the simulation and (B) from the experiment.

defined as the temperature rise above the equilibrium temperature. The thermal response is much slower at several hundreds of nanometers from the NP than that near it (where it is submicrosecond), Figure 1A. Consequently, after 2 μs the approach to a steady state is evident near the NP, while far from the NP the dT values are still growing. These observations are useful for interpreting our results qualitatively. Because the change in total detected power due to the photothermal effect comes from scattering at different locations within the dynamic thermal lens and peripheral locations in the probe beam receive the heat from the source with a time lag, the detected signal is initially expected to come mainly from locations close to the NP (and at the center of the probe beam) while contributions from the larger shell volume at the periphery of the probe beam become significant later.

We next examine the limiting cases of homogeneous states (all solid or all liquid SA). To this end, experiments were performed at different stage chamber temperatures, either well below the melting temperature or above it. Figure 2A,B presents the time evolution of experimental and computed PT signals for the two homogeneous media. The plotted PT signals are defined as the change in the detected power of the probe beam, $P_{probe}(t)$, normalized by its value before the heating pulse: $[P_{probe}(t) - P_{probe}(0)]/P_{probe}(0)$, with the distant detector subtending a small angle about the forward direction. The duty cycle was chosen so that after each heating pulse there was enough time to reach the equilibrium defined by the specific initial temperature. We used 30 °C for solid SA and 80 °C for liquid SA. The heating power was P_h = 1 mW, which corresponds to an estimated maximum temperature rise at the NP surface, $\Delta T_{NP}^{(max)}$, of 17.5 and 40.5 °C when the surrounding SA is in solid and liquid phases, respectively. The connection between P_h and $\Delta T_{NP}^{(max)}$ goes through Q_h, the rate at which the NP absorbs energy from the heating beam. Q_h is calculated by treating the beam as a scalar, Gaussian wave and using Mie theory for an absorption cross-section. The relation between Q_h and $\Delta T_{NP}^{(max)}$ is determined by using the analytic, steady-state temperature profile. Our heat pulses are too short for the system to reach a full steady state so the $\Delta T_{NP}^{(max)}$ acts as an upper bound on the NP temperature rise. In a single phase system with spherical symmetry one has the approximate, but explicit, simple result:[50]

$$\Delta T_{NP}^{(max)} \approx \frac{Q_h}{4\pi\kappa R} \quad (1)$$

where κ is the SA thermal conductivity and R is the NP radius. A more detailed description of this analysis is given in the Supporting Information.

Because of the negative thermorefractive index coefficient in both solid and liquid states, the local rise in temperature induces the formation of a spherical diverging nanolens.[22,51,52] In our experiments, the focal plane of the probe beam is located in front of the NP (which sits also beyond the focus of the heating beam). Thus, the effect of the thermal nanolens is to make the rays impinging on the detector more divergent, yielding a reduced $P_{probe}(t)$ and a negative PT signal. This prediction was confirmed by both the thermo-optical simulation and experiment, Figure 2A,B.

Considering first the simulation results, we found that dT_{NP} for the liquid phase was always greater than dT_{NP} for the solid phase. This behavior is due to the lower thermal conductivity of the liquid (see Table 1). In support of this claim, note that at the end of heating the ratio of dT_{NP} values (liquid over solid) is 2.31, which is close to the inverse ratio of the thermal conductivities, 2.37. The reason for this coincidence comes from assuming near steady state conditions and applying eq 1 for a common value of Q_h to the two separate phases.[22] Since liquid SA also has a stronger temperature dependence of its optical refractive index than the solid, see Table 1 and Figure 2D, it follows that the ratio of dn/dT values (liquid over solid) is 3.528/2.397 = 1.47. One might then expect that the ratio of the PT signals (liquid over solid) at 2 μs would be close to 2.37 × 1.47 = 3.48. However, from Figure 2B the ratio from simulations is only 2.05. We attribute this discrepancy to the assumption of a full steady state having been reached everywhere at 2 μs, which increasingly fails for material farther away from the NP. This feature is also implied by the slower varying PT signals compared to the much more abrupt kinetics of the temperature and index of refraction changes at the surface of the NP (Figure 2C,D). The lack of steady state behavior also differs between the phases as shown in Figure 2B where the liquid's PT signal exhibits less saturation at t = 2 μs than the solid's. These observations reiterate the idea of the PT signal representing a weighted average of optothermal changes through the entire probe volume, as discussed earlier.

Figure 2A,B shows good qualitative agreement between the optothermal numerical simulation and experimental results in homogeneous media. In terms of signal magnitude, the difference between calculated and the experimental values for the solid phase is only 5%. For the liquid state, however, the difference in magnitude is more pronounced (41%). The origin of this quantitative discrepancy is unclear at the moment. It could be due to SA thermal and optical parameters differing from those in Table 1 or due to particle size/shape experimental uncertainties. A further possibility that we have considered is that in our simulations we have neglected the thermal contribution of the substrate glass. When SA is in

https://doi.org/10.1021/acsnano.2c09212
ACS Nano 2023, 17, 505−514

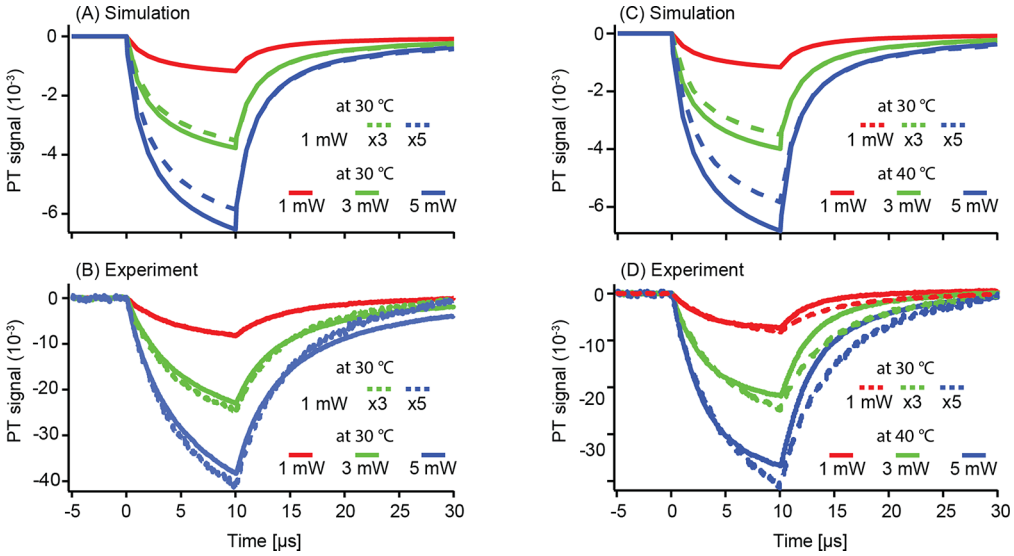

Figure 4. Comparison between the time-resolved PT signals measured at P_h = 1, 3, 5 mW (solid lines) and amplified signals obtained by multiplying by 3 or 5 the PT signal at P_h = 1 mW with a starting temperature of 30 °C mW (dashed lines): (A, B) from a starting temperature 30 °C; (C, D) from a starting temperature of 40 °C.

liquid state, particles are adsorbed onto the glass substrate. The substrate should primarily lower the liquid PT signal, which is the opposite of the observed increase with respect to the simulation. The thermal conductivity of glass is ~2.5 times that of solid SA and 6 times that of liquid SA. In terms of heat flow, the glass provides a thermal "short circuit". Therefore, including the effect of the substrate in the calculations is unlikely to solve this discrepancy. In terms of kinetics, we note that during cooling, the PT signal falls in similar relative amounts in computations as well as experiment for both liquid and solid phases. At this point we consider the qualitative agreement sufficiently encouraging to warrant moving to the next step, which is to determine whether a finite phase transition can be observed in an experiment where one starts with a solid medium, delivers enough heat for melting, then lets it cool and solidify back to the initial state.

When thermal parameters are temperature independent, the time evolution of heat diffusion can only vary linearly with the magnitude of the absorbed optical power. This result is why we did not need to state the incident power used in producing Figure 1. However, the optical scattering has a linear dependence on Q only if the scattering is weak, i.e., only if the PT signal is small. We first examined the extent that this behavior holds for liquid SA, when the power of the heating pulse is swept from 1 to 6 mW. For Figure 3 (and successive figures), we made several additional changes in the experimental conditions. All the data were collected using a single NP, and the heating pulse length was increased to 10 μs. To enhance PT signal strengths, the probe focal plane was moved farther (13 μm) from the NP and its incident power, P_p, raised to 17.4 mW. Although its wavelength is far from the gold NP absorption resonance, the larger value of P_p makes its heating effect comparable to that of the heating beam with P_h = 1 mW. The probe beam is not pulsed so in each cycle for Figure 3 the system starts and ends with the steady state solution in the liquid characterized by $\Delta T_{NP}^{(max)}$ = 21.64 °C due to the probe beam. For comparison, the heating beam with P_h = 1 mW has by itself a $\Delta T_{NP}^{(max)}$ = 29.97 °C. The combined effect of the two beams when P_h = 6 mW has a bound of $\Delta T_{NP}^{(max)}$ = 188.7 °C. The calculations of these temperature bounds and the reversibility of experimental observations ensure us that the temperature never reaches the SA boiling temperature (361 °C) during the measurements.

To test the invariance of dynamics with the optical absorbed power, we compared the PT signal measured at different heating powers (say n mW) with an "amplified" signal obtained by multiplying the PT signal at 1 mW by n. Results from this algorithm are shown in Figure 3A,B. Note that the discrepancy between PT signal magnitudes in simulations and experiment, discussed above for Figure 2A,B, has grown to be about five. Hence we concentrate on the qualitative comparisons between the two, basically ignoring the vertical axis scales. At low heating powers, in both simulations and experiments, the extrapolated and measured PT signals overlap to a satisfactory extent. At the highest power, the overlap between experimental (but not simulated) waveforms is less. Since a strong overlap is an indication of linearity of both optical and thermal responses, it follows that, if the medium is not described by a linear model, the overlapping should not happen. Such nonlinear behavior could be caused by the temperature dependence of the thermal parameters, by effects arising from finite optical apertures (at high power), and by phase transitions. We are interested in revealing the last.

To this end, in the following we compare the measured PT signals, under conditions where a solid−liquid phase change is expected to occur reversibly, to the amplified signals using P_h = 1 mW with a starting temperature low enough that the SA does not melt. Thus, it represents the thermal time evolution in the absence of a phase change. In these phase change experiments, the temperature before the heating pulse is everywhere below the melting temperature, while enough energy is absorbed to exceed the SA melting temperature at the NP surface for P_h above a threshold. For example, with an initial temperature of 30 °C, the bound on the probe beam's effect on the solid phase is $\Delta T_{NP}^{(max)}$ = 9.13 °C, while the combined effect of $Q = Q_p + Q_h$ with Q_h = 1 mW on the solid phase is $\Delta T_{NP}^{(max)}$ = 21.78 °C. Both of these bounds are less than 69.3 − 30 = 39.3 °C so there will be no melting. A phase transition does not become possible with this initial temperature until P_h exceeds 3 mW. At the other extreme, to satisfy our conditions when P_h = 6 mW,

https://doi.org/10.1021/acsnano.2c09212
ACS Nano 2023, 17, 505−514

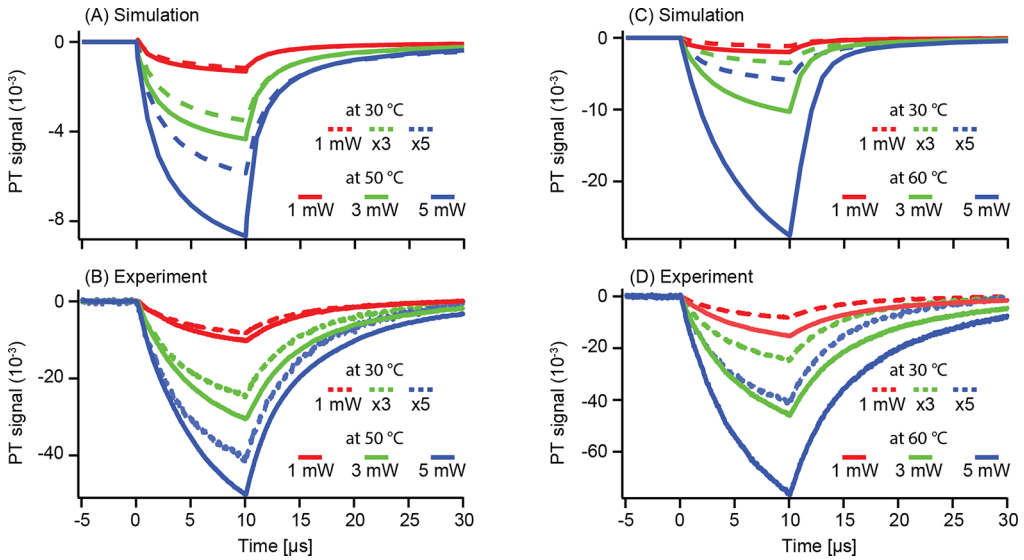

Figure 5. Comparison between the time-resolved PT signals measured at P_h = 1,3,5 mW (solid lines) and amplified signals obtained by multiplying by 1, 3 or 5 the PT signal at P_h = 1 mW with a starting temperature of 30 °C (dashed lines): (A, B) from a starting temperature of 50 °C; (C, D) from a starting temperature of 60 °C.

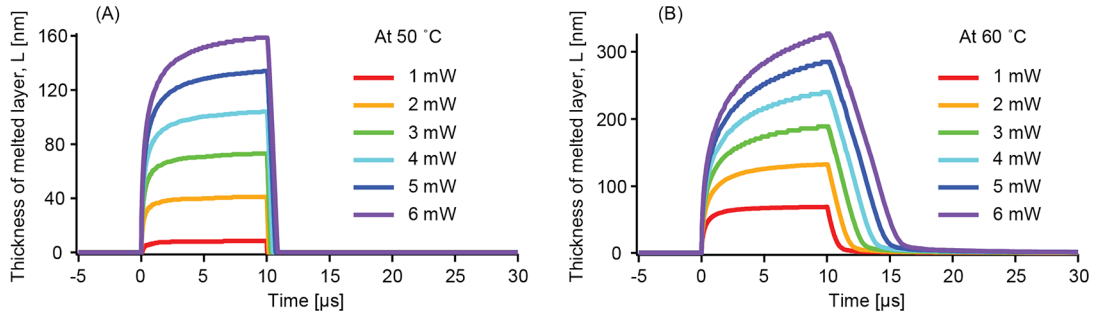

Figure 6. Calculated thickness of the melted layer as a function of time for a 10 μs square heating pulse at (A) 50 °C and (B) 60 °C.

we must keep the starting temperature less than 69.3 − 9.13 = 60.17 °C.

Figure 4 shows applications of our algorithm for initial temperatures of 30 and 40 °C. Simulated comparisons of measured and amplified PT signals at 10 μs for different heating powers predict maximum deviations of ∼5% at P_h = 3 mW and ∼15% at P_h = 5 mW for a starting temperature of 30 °C. These maximum deviations nearly double in size for a starting temperature of 40 °C. However, the observed deviations in the experiment are opposite to those predicted by simulations when the starting temperature is 30 °C but nearly absent when the starting temperature is 40 °C. In addition there are significant deviations at long cooling times for both starting temperatures. All of these experimental deviations have a smaller or similar magnitude (<10%) to those observed in Figure 3 for the homogeneous liquid SA. It is worth noting here that with 3 or 4 mW of heating power, the maximum thickness of the melted liquid layers was calculated to be 11.5 or 30.3 nm, respectively. Compared to the size of the probed volume (several μm^3), these liquid volumes are very small. As a consequence, it is reasonable to assume that the differences between amplified waveforms and the data have the same origins as those discussed in regard to the liquid state in Figure 3.

When the gap between the environmental temperature and the melting temperature is narrower and therefore when the phase transition is more generously allowed, the differences between the homogeneous medium reference and the actual data become larger, Figure 5. Specifically, signals calculated with accounting for phase changes and an initial temperature of 50 °C (Figure 5A) predict (i) a lack of overlapping with their corresponding extrapolated reference waveforms and (ii) a larger magnitude for the phase-change signals than that of their homogeneous medium reference waveforms. Indeed the measured PT signals (Figure 5B) are consistent with both these predictions. At 60 °C, the trends become even more obvious. Note too that even with P_h = 1 mW there is a lack of overlap for both starting temperatures, consistent with our estimates of when a phase transition is possible. There is qualitative agreement between simulation and experiment. Thus, based on the much larger magnitude of deviations (20−30%) than in the previous cases (Figures 3 and 4), we attribute the breakdown of the linear response behavior to a reversible phase change. Figure S4 in the Supporting Information shows similar behavior for a starting temperatures of 50, 60 °C with P_h = 2, 4, 6 mW.

We note that despite overall good agreement between simulations including a phase change and experimental PT data, there are also some discrepancies, which are specific to the phase change regime (i.e., are not present in the homogeneous medium PT experiments, Figure 2). Specifically, it takes longer to recover the base level in the experiment,

https://doi.org/10.1021/acsnano.2c09212
ACS Nano 2023, 17, 505−514

Figure 5. This discrepancy is potentially due to the omission of supercooling/nucleation effects in our calculations. Improving the model as well as obtaining quantitative agreement between experiment and simulations will have to be addressed in the future. However, within the demonstrated limits of our approach, one can still gain an idea about the overall characteristics of phase change dynamics by examining the simulated melting as a function of time, Figure 6.

We consider two initial temperatures (50 and 60 °C) used in experiments with heating powers between 1 and 6 mW and plot L, the thickness of the melted layer, versus time. The liquid shell (assumed spherical in the simulations) forms rapidly (~0.1 m/s) at the beginning of the pulse. Its growth slows as it approaches a steady state thickness value which depends on the heating power and the initial temperature. Under the same heating power, we expected the maximum value of L to be greater for a starting temperature of 60 °C, as the system requires less energy to reach the melting point. An expression for the steady state value of L is given in the Supporting Information. At cooling, the larger the value of L that has been reached by the end of the heat pulse, the slower is the return to the initial (solid) state. This behavior is most evident in Figure 6B. The qualitative reason for the slower freezing rate for larger L values is the need for the SA to release a greater amount hot-liquid thermal energy and latent heat.

Putting together the results discussed so far leads to the following picture, Figure 7. When the heating is turned on at t = 0, the temperature at the surface of the gold NP immediately starts increasing rapidly. Farther from the particle, the increase is more gradual (contrast temperatures in Figure 7 at r = 50 nm and r = 200 nm). As temperatures begin to exceed the bulk melting point, the phase change initiates and the solid/liquid interface starts moving outward at initial speeds of tens of cm/s. Depending on the location, a kink can be observed in the temperature versus time curves. See Supporting Information Figures S5 and S6 for a closer look at several examples. This is usually due to the solid/liquid interface passing through that specific position. Before that time the heating rate there has been reduced due to latent heat being absorbed and temperature paused at locations nearer the NP. After the solid/liquid interface moves beyond the position, the temperature rise accelerates because latent heat effects no longer limit heat flow to the location plus the material there is now liquid, which has a smaller thermal conductivity than solid SA. When the heating pulse stops, cooling starts as heat dissipates through the medium. The initial cooling is very rapid, with rates of ~10^8 °C/s, and is mostly due to the hot liquid. However, once freezing begins, cooling slows down as latent heat is released during resolidification. This leads to a shoulder in the dT vs t curves and a roughly linear decrease of L back to zero. In the absence of supercooling, the solidification front was calculated to travel back toward the nanoparticle at an estimated 10 cm/s. Cooling of the restored solid phase is marked first by the sudden drop in the dT curves, since latent heat is no longer being released, followed by a slow decay of dT in the solid SA back to the steady state produced by the probe beam. Many of these described structures in the dT curves do not carry over to plots of PT signals versus time; see Figure S7 in the Supporting Information. This is again a consequence of the PT signal being determined by scattering throughout the domain of temperature changes.

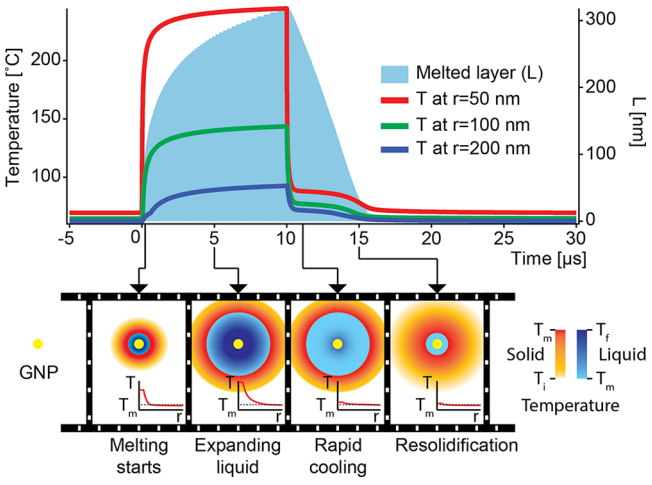

Figure 7. Temperature time evolution at r = 50 (red), 100 (green), and 200 (blue) nm and time-dependent thickness of the melted layer (L), for 6 mW of heating with 60 °C initial temperature.

The phase change kinetic model on which the above picture is based is the simplest conceivable. It does not take into account nucleation, supercooling, interfacial thermal resistance, the curvature (Gibbs–Thomson) effect, the influence of impurities on the liquid–solid interface shape, and velocity. Nevertheless, together with the experimental/computational workflow presented here, it provides a groundwork from which to start building better models that will allow studying these interesting phenomena.

CONCLUSION

We have introduced a combined theoretical and experimental methodology to investigate the time behavior of phase transformations induced in a medium by light absorbing nanoparticles. The experimental approach involved low-duty-cycle pulsed heating of nanoparticles embedded in a transparent medium and averaging over many pulses the periodic change in the optical power of a focused probe beam due to photothermal effects. As a proof of principle, we have studied the kinetics of transient melting and refreezing of stearic acid in the vicinity of spherical Au nanoparticles. We estimated the rates of resolidification and cooling by comparing experimental data with simulations. Because of interfacial and geometric effects, kinetics of such phase transitions promoted by nanoparticles could be starkly different from bulk behavior. The approach should prove helpful in measuring such differences, in studies seeking a better understanding of nonequilibrium phase changes at nanoscale.

METHODS

Sample Preparation. A borosilicate cover glass (catalog no. 72210-10, Electron Microscopy Sciences) was coated by the drop casting method with 20 μL of citrate-stabilized gold-nanospheres solution (OD 1, diameter = 100 nm, product no. 15711-20, TED PELLA, Inc.) diluted 1:4 with purified water (Direct-Q 3, MilliporeSigma). An approximately 5 mg flake of stearic acid (CAS 57-11-4, 90% purity, Sigma-Aldrich) was placed on top of the coated cover glass which was then gently transferred into a nitrogen-filled temperature-controllable sample stage (HCS321Gi-mK2000, INSTEC, Inc.). The sample stage is a double-sealed chamber, which enables accurate control of the ambient temperature with high precision (0.01 °C) and 0.05 °C of long-term stability, within a range from −80 to 250 °C. The cover glass was heated up to 80 °C until the

https://doi.org/10.1021/acsnano.2c09212
ACS Nano 2023, 17, 505−514

SA flake melted completely, while the melting process was monitored with bright-field microscopy. The liquid SA was then covered with another cover glass for protection from external contamination and uniform thickness of the SA layer. It should be noted that a fraction of the SA initially put on the bottom cover glass flowed out of the sandwiched layer, so the thickness of the SA layer was measured afterward. From the axial positions of the illumination objective lens along with the optical axis at which it provides the maximum reflectance of the heating beam from the interfaces, we measured the thickness of the SA layer (~100 μm). Lastly, the sample was cooled down to room temperature slowly (−1 °C/min) for solidification of the SA. The spatial and size distributions of the NPs were evaluated using photothermal heterodyne imaging (PHI) with the intensity histogram of the PHI signal measured with a lock-in amplifier and a sinusoidally modulated heating beam at 30 kHz. (See Figure S2 for an example of PHI map used to obtain intensity histograms of single particle signals.)

Time-Resolved Microscopy. The experimental apparatus for the measurement of the PT signal was based on a home-built laser-scanning microscopy (Figure S1). This analytical method employed two CW laser light sources at wavelengths of 532 and 785 nm as the heating and probe beams, respectively. The wavelengths were chosen to be close to or far from the strongest peak of the absorption spectrum of the gold NP, for efficient plasmonic excitation by the heating beam or for possibly less heating by the probe beam. The intensity of the heating beam was modulated in time to be a rectangular pulse by an acousto-optic modulator (35250-.2-.53-XQ, Sintec Optronics). The time duration of each heating pulse was 2 or 10 μs, with ~50 ns of rise and fall times, repeated at a frequency of 200 Hz. The beams were combined and then guided by a galvanometer mirror scanner (GVS012, Thorlabs, Inc.) for lateral scanning of the backscattered dark-field imaging or the epi-detected PHI. Owing to the spatial gap between the sample and the outer window of the sample stage (5.27 mm), we used a long working distance objective lens (Plan Apo 100× LWD, NA 0.7, WD 6 mm, Mitutoyo) for focused illumination of the beams. Transient changes of the intensity of the probe beam were monitored by a fiber-coupled fast detector (SV2-FC, Thorlabs, Inc.) in the forward direction, which allowed real-time optical measurements with 150 ps of rise/fall time. Finally, the time-resolved PT signals were collected and averaged over 2000 pulses by a fast digital oscilloscope (WaveSurfer 432, 2 GSa/s, LeCroy) for improvement of the signal-to-noise ratio. More details of the optical setup are available in the Supporting Information. A particular challenge of our detection scheme was finding a NP that did not shift its lateral location (modifying the detected probe signal) over the course of the many melting/refreezing cycles.

Numerical Simulation. We built two numerical simulation models based on the finite element method in COMSOL Multiphysics. The first was for the calculation of transient conductive heat dissipation with the NP as a source, with or without phase changes being possible in the surrounding material. Its key approximation was the assumption that the NP is in a spherically symmetric environment, completely surrounded by SA, while the experimental configuration had the NP sitting on a cover glass with a second cover glass ~100 μm above it. This assumption implies that the temperature distribution could only depend on the radial coordinate, which significantly shortened calculation times and reduced data storage. We also ignored the ~11% density difference between solid and liquid SA. Although these assumptions have quantitative implications, the important features observed in the experiments were qualitatively reproduced by the simulations. The second model solved Maxwell's equations for the scattering and propagation of the probe beam, providing the real-time change of the beam's power onto the detector. The time, space, and phase dependent distributions of SA optical properties needed for this model were found by combining the data in Table 1 for the temperature and phase dependence of SA's indices of refraction with the results from the heat diffusion model. See the Supporting Information for more details of these models.

ASSOCIATED CONTENT

Supporting Information

The Supporting Information is available free of charge at https://pubs.acs.org/doi/10.1021/acsnano.2c09212.

Detailed descriptions about the experimental PT microscope setup and computational model for the calculation of heat transfer and optical scattering and supplemental Figures S1−S7 supporting the main text (PDF)

AUTHOR INFORMATION

Corresponding Author

Bogdan Dragnea − *Department of Chemistry, Indiana University, Bloomington, Indiana 47405, United States;* orcid.org/0000-0003-0611-2006; Phone: +1 812-856-0087; Email: dragnea@indiana.edu

Authors

Suhun Jo − *Department of Chemistry, Indiana University, Bloomington, Indiana 47405, United States*

William L. Schaich − *Department of Physics, Indiana University, Bloomington, Indiana 47405, Unites States*

Complete contact information is available at: https://pubs.acs.org/10.1021/acsnano.2c09212

Notes

The authors declare no competing financial interest.

ACKNOWLEDGMENTS

The authors gratefully acknowledge support for this work from the National Science Foundation, Awards 1808027 and 2107664.

REFERENCES

(1) Holmberg, V. C.; Panthani, M. G.; Korgel, B. A. Phase transitions, melting dynamics, and solid-state diffusion in a nano test tube. *Science* **2009**, *326*, 405−407.

(2) Wettlaufer, J.; Worster, M. G. Premelting dynamics. *Annu. Rev. Fluid Mech.* **2006**, *38*, 427−452.

(3) Neumann, O.; Urban, A. S.; Day, J.; Lal, S.; Nordlander, P.; Halas, N. J. Solar vapor generation enabled by nanoparticles. *ACS Nano* **2013**, *7*, 42−49.

(4) Meister, K.; Strazdaite, S.; DeVries, A. L.; Lotze, S.; Olijve, L. L.; Voets, I. K.; Bakker, H. J. Observation of ice-like water layers at an aqueous protein surface. *Proc. Natl. Acad. Sci. U. S. A.* **2014**, *111*, 17732−17736.

(5) Deming, J. W.; Eicken, H. In *Planets and Life: The Emerging Science of Astrobiology*; Sullivan, W. T., III, Baross, J., Eds.; Cambridge University Press, 2007; Chapter 15, pp 292−312.

(6) Ruiz Pestana, L.; Felberg, L. E.; Head-Gordon, T. Coexistence of Multilayered Phases of Confined Water: The Importance of Flexible Confining Surfaces. *ACS Nano* **2018**, *12*, 448−454.

(7) Slater, B.; Michaelides, A. Surface premelting of water ice. *Nat. Rev. Chem.* **2019**, *3*, 172−188.

(8) Ross, F. M. Opportunities and challenges in liquid cell electron microscopy. *Science* **2015**, *350* (6267), 1490.

(9) Wang, X.; Yang, J.; Andrei, C. M.; Soleymani, L.; Grandfield, K. Biomineralization of calcium phosphate revealed by in situ liquid-phase electron microscopy. *Commun. Chem.* **2018**, *1*, 80.

(10) Brown, B. S.; Hartland, G. V. Influence of Thermal Diffusion on the Spatial Resolution in Photothermal Microscopy. *J. Phys. Chem. C* **2022**, *126*, 3560−3568.

(11) Yang, B.; Li, C.; Wang, Z.; Dai, Q. Thermoplasmonics in Solar Energy Conversion: Materials, Nanostructured Designs, and Applications. *Adv. Mater.* **2022**, *34*, 2107351.

(12) Bundschuh, M.; Filser, J.; Lüderwald, S.; McKee, M. S.; Metreveli, G.; Schaumann, G. E.; Schulz, R.; Wagner, S. Nanoparticles in the environment: where do we come from, where do we go to? *Environ. Sci. Eur.* **2018**, *30*, 6.
(13) Carslaw, K.; Boucher, O.; Spracklen, D.; Mann, G.; Rae, J.; Woodward, S.; Kulmala, M. A review of natural aerosol interactions and feedbacks within the Earth system. *Atmos. Chem. Phys.* **2010**, *10*, 1701−1737.
(14) Conca, K.; Thwaites, J.; Lee, G. Climate change and the UN Security Council: bully pulpit or bull in a china shop? *Global Environ. Politics* **2017**, *17*, 1−20.
(15) National Academies of Sciences, Engineering, and Medicine. *Reflecting Sunlight: Recommendations for Solar Geoengineering Research and Research Governance*; The National Academies Press: Washington, DC, 2021.
(16) Dicken, M. J.; Aydin, K.; Pryce, I. M.; Sweatlock, L. A.; Boyd, E. M.; Walavalkar, S.; Ma, J.; Atwater, H. A. Frequency tunable near-infrared metamaterials based on VO 2 phase transition. *Opt. Express* **2009**, *17*, 18330−18339.
(17) Pustovalov, V.; Smetannikov, A.; Zharov, V. Photothermal and accompanied phenomena of selective nanophotothermolysis with gold nanoparticles and laser pulses. *Laser Phys. Lett.* **2008**, *5*, 775−792.
(18) Li, H.; Xu, S.; Quan, J.; Yung, B. C.; Pang, J.; Zhou, C.; Cho, Y.-A.; Zhang, M.; Liu, S.; Muthusamy, N.; et al. CD33-Targeted lipid nanoparticles (aCD33LNs) for therapeutic delivery of GTI-2040 to acute myelogenous leukemia. *Mol. Pharmaceutics* **2015**, *12*, 2010−2018.
(19) Barreneche, C.; Martín, M.; Calvo-de la Rosa, J.; Majó, M.; Fernández, A. I. Own-synthetize nanoparticles to develop nano-enhanced phase change materials (NEPCM) to improve the energy efficiency in buildings. *Molecules* **2019**, *24*, 1232.
(20) Adhikari, S.; Spaeth, P.; Kar, A.; Baaske, M. D.; Khatua, S.; Orrit, M. Photothermal microscopy: imaging the optical absorption of single nanoparticles and single molecules. *ACS Nano* **2020**, *14*, 16414−16445.
(21) Berciaud, S.; Cognet, L.; Blab, G. A.; Lounis, B. Photothermal heterodyne imaging of individual nonfluorescent nanoclusters and nanocrystals. *Phys. Rev. Lett.* **2004**, *93*, 257402.
(22) Selmke, M.; Braun, M.; Cichos, F. Photothermal single-particle microscopy: detection of a nanolens. *ACS Nano* **2012**, *6*, 2741−2749.
(23) Nedosekin, D. A.; Galanzha, E. I.; Dervishi, E.; Biris, A. S.; Zharov, V. P. Super-resolution nonlinear photothermal microscopy. *Small* **2014**, *10*, 135−142.
(24) Koh, E. S.; McDonald, J.; Tsvetkova, I. B.; Dragnea, B. Measurement of nanoparticle adlayer properties by photothermal microscopy. *J. Phys. Chem. Lett.* **2015**, *6*, 3621−3625.
(25) Gaiduk, A.; Yorulmaz, M.; Ruijgrok, P.; Orrit, M. Room-temperature detection of a single molecule's absorption by photothermal contrast. *Science* **2010**, *330*, 353−356.
(26) Celebrano, M.; Kukura, P.; Renn, A.; Sandoghdar, V. Single-molecule imaging by optical absorption. *Nat. Photonics* **2011**, *5*, 95−98.
(27) Baffou, G.; Polleux, J.; Rigneault, H.; Monneret, S. Super-heating and micro-bubble generation around plasmonic nanoparticles under cw illumination. *J. Phys. Chem. C* **2014**, *118*, 4890−4898.
(28) Karabutov, A. A.; Savateeva, E. V.; Oraevsky, A. A.Optoacoustic supercontrast for early cancer detection. *Biomedical Optoacoustics II*, BiOS 2001 The International Symposium on Biomedical Optics, San Jose, CA, United States, June 15, 2001; Proceedings Volume 4256; SPIE, 2001; pp 179−187, DOI: 10.1117/12.429306.
(29) Zharov, V. P.; Letfullin, R. R.; Galitovskaya, E. N. Microbubbles-overlapping mode for laser killing of cancer cells with absorbing nanoparticle clusters. *J. Phys. D: Appl. Phys.* **2005**, *38*, 2571−2581.
(30) Hou, L.; Yorulmaz, M.; Verhart, N. R.; Orrit, M. Explosive formation and dynamics of vapor nanobubbles around a continuously heated gold nanosphere. *New J. Phys.* **2015**, *17*, 013050.
(31) Dykman, L.; Khlebtsov, N. Gold nanoparticles in biomedical applications: recent advances and perspectives. *Chem. Soc. Rev.* **2012**, *41*, 2256−2282.
(32) Lukianova-Hleb, E. Y.; Ren, X.; Townley, D.; Wu, X.; Kupferman, M. E.; Lapotko, D. O. Plasmonic nanobubbles rapidly detect and destroy drug-resistant tumors. *Theranostics* **2012**, *2*, 976.
(33) Lukianova-Hleb, E.; Hu, Y.; Latterini, L.; Tarpani, L.; Lee, S.; Drezek, R. A.; Hafner, J. H.; Lapotko, D. O. Plasmonic nanobubbles as transient vapor nanobubbles generated around plasmonic nanoparticles. *ACS Nano* **2010**, *4*, 2109−2123.
(34) Teirlinck, E.; Xiong, R.; Brans, T.; Forier, K.; Fraire, J.; Van Acker, H.; Matthijs, N.; De Rycke, R.; De Smedt, S. C.; Coenye, T.; Braeckmans, K. Laser-induced vapour nanobubbles improve drug diffusion and efficiency in bacterial biofilms. *Nat. Commun.* **2018**, *9*, 4518.
(35) Raes, L.; Stremersch, S.; Fraire, J. C.; Brans, T.; Goetgeluk, G.; De Munter, S.; Van Hoecke, L.; Verbeke, R.; Van Hoeck, J.; Xiong, R.; et al. Intracellular delivery of mRNA in adherent and suspension cells by vapor nanobubble photoporation. *Nano-Micro Lett.* **2020**, *12*, 185.
(36) Xiong, R.; Raemdonck, K.; Peynshaert, K.; Lentacker, I.; De Cock, I.; Demeester, J.; De Smedt, S. C.; Skirtach, A. G.; Braeckmans, K. Comparison of gold nanoparticle mediated photoporation: vapor nanobubbles outperform direct heating for delivering macromolecules in live cells. *ACS Nano* **2014**, *8*, 6288−6296.
(37) Lombard, J.; Biben, T.; Merabia, S. Kinetics of Nanobubble Generation Around Overheated Nanoparticles. *Phys. Rev. Lett.* **2014**, *112*, 105701.
(38) Parra-Vasquez, A. N. G.; Oudjedi, L.; Cognet, L.; Lounis, B. Nanoscale thermotropic phase transitions enhancing photothermal microscopy signals. *J. Phys. Chem. Lett.* **2012**, *3*, 1400−1403.
(39) Heber, A.; Selmke, M.; Cichos, F. Metal nanoparticle based all-optical photothermal light modulator. *ACS Nano* **2014**, *8*, 1893−1898.
(40) Zahedian, M.; Lee, Z.; Koh, E. S.; Dragnea, B. Studies of Nanoparticle-Assisted Photoannealing of Polydimethylsiloxane by Time-Harmonic Photothermal Microscopy. *ACS Photonics* **2020**, *7*, 2601−2609.
(41) Lu, L.; Cai, J.; Frost, R. L. Near infrared spectroscopy of stearic acid adsorbed on montmorillonite. *Spectrochim. Acta, Part A* **2010**, *75*, 960−963.
(42) Fu, X.; Liu, Z.; Wu, B.; Wang, J.; Lei, J. Preparation and thermal properties of stearic acid/diatomite composites as form-stable phase change materials for thermal energy storage via direct impregnation method. *J. Therm. Anal. Calorim.* **2016**, *123*, 1173−1181.
(43) National Center for Biotechnology Information (2022), PubChem Substance Record for SID 316963273, 57-11-4. https://pubchem.ncbi.nlm.nih.gov/substance/316963273 (accessed August 2022).
(44) Lide, D. R., Ed. *CRC Handbook of Chemistry and Physics*; CRC Press, Inc.: Boca Raton, FL, 2004; Vol. *85*.
(45) Schaake, R.; Van Miltenburg, J.; De Kruif, C. Thermodynamic properties of the normal alkanoic acids II. Molar heat capacities of seven even-numbered normal alkanoic acids. *J. Chem. Thermodyn.* **1982**, *14*, 771−778.
(46) Bayram, Ü.; Aksöz, S.; Maraşlı, N. Temperature dependency of thermal conductivity of solid phases for fatty acids. *J. Therm. Anal. Calorim.* **2014**, *118*, 311−321.
(47) Johnson, J. F. Phase transformations in commercial paraffin waxes. *Industrial & Engineering Chemistry* **1954**, *46*, 1046−1048.
(48) Cedeño, F. O.; Prieto, M. M.; Xiberta, J. Measurements and estimate of heat capacity for some pure fatty acids and their binary and ternary mixtures. *J. Chem. Eng. Data* **2000**, *45*, 64−69.
(49) Vargaftik, N. B.*Handbook of Thermal Conductivity of Liquids and Gases*; CRC Press, Inc.: Boca Raton, FL, 1993.
(50) Govorov, A. O.; Zhang, W.; Skeini, T.; Richardson, H.; Lee, J.; Kotov, N. A. Gold nanoparticle ensembles as heaters and actuators: melting and collective plasmon resonances. *Nanoscale Res. Lett.* **2006**, *1*, 84−90.

(51) Cassano, C. L.; Mawatari, K.; Kitamori, T.; Fan, Z. H. Thermal lens microscopy as a detector in microdevices. *Electrophoresis* **2014**, *35*, 2279−2291.
(52) Uchiyama, K.; Hibara, A.; Kimura, H.; Sawada, T.; Kitamori, T. Thermal lens microscope. *Jpn. J. Appl. Phys.* **2000**, *39*, 5316.

https://doi.org/10.1021/acsnano.2c09212
ACS Nano 2023, 17, 505−514